Available online at www.sciencedirect.com

ScienceDirect

Advances in Space Research 71 (2023) 1840–1854

ADVANCES IN SPACE RESEARCH (a COSPAR publication)

www.elsevier.com/locate/asr

Magnetic connectivity and solar energetic proton event intensity profiles at deka-MeV energy

Miikka Paassilta [a,*], Rami Vainio [a], Athanasios Papaioannou [b], Osku Raukunen [a,c], Suvi Barcewicz [a], Anastasios Anastasiadis [b]

[a] Department of Physics and Astronomy, University of Turku, 20014, Finland

[b] Institute for Astronomy, Astrophysics, Space Applications and Remote Sensing (IAASARS), National Observatory of Athens, I. Metaxa & Vas. Pavlou St. GR-15236, Penteli, Greece

[c] Aboa Space Research Oy, Tierankatu 4, 20520 Turku, Finland

Received 17 May 2022; received in revised form 26 October 2022; accepted 26 November 2022
Available online 5 December 2022

Abstract

We present an analysis of the time-intensity profiles of 25 solar energetic proton events at 18.2 MeV, modelled by fitting an analytical function form (a modified Weibull function) to the observed intensities. Additionally relying on previous work that characterized the magnetic connectivity between the event-related solar flare and the observer in these events with three angular parameters, we investigate the fit function parameters, the connectivity parameters, and the iron-to-carbon ratio of the events for dependencies and correlations. We find that the fit parameter controlling the basic shape of the profile (parameter a) is not clearly dependent on the connectivity parameters or the Fe/C ratio, suggesting that the profile shapes of neither well and weakly connected nor generally "impulsive" and "gradual" events differ systematically during the early stages of the event at 1 AU. In contrast, the time scaling of the fit function (parameter b) is at least moderately correlated with both the magnetic connectivity parameters and the Fe/C ratio, in that well-connected and iron-rich events are typically shorter in relative duration than weakly connected and nominal-abundance events; intensity rise times display a similar correlation with the connectivity parameters. We interpret the former result as following from the combined effect of various transport processes acting on the particles in interplanetary space, while the latter is essentially consistent with established knowledge regarding the observed dependence of the time-intensity profile shapes of solar energetic particle events on their magnetic connectivity and heavy ion abundances. The desirability of modelling the particle transport effects in detail and extending the analysis to cover higher energies is indicated.

Keywords: Sun: abundances; Sun: particle emission

1. Introduction

Solar energetic particle (SEP) events occur as a result of eruptive discharges of energy stored in magnetic fields at and near the surface of the Sun (Reames, 2013). Because they can provide insight into particle acceleration and propagation processes, they are an object of intensive study. Events involving heavy particles of high kinetic energies, primarily protons and other ions with E $\gtrsim$ 10 MeV/nucleon, are of interest also due to their significance for space weather and potentially detrimental impact on space missions, as well as the human society at large (e.g. Vainio et al., 2009; Mishev, 2014; Papaioannou et al., 2016).

A wide variety of physical processes and conditions determine and affect the maximum intensity, duration

* Corresponding author.
E-mail addresses: mimapa@utu.fi (M. Paassilta), rami.vainio@utu.fi (R. Vainio), atpapaio@astro.noa.gr (A. Papaioannou), oajrau@utu.fi (O. Raukunen), anastasi@noa.gr (A. Anastasiadis).

https://doi.org/10.1016/j.asr.2022.11.051
0273-1177/

and the overall form of the time-intensity profile of any given SEP event as observed at a distance from the Sun. Aside from the initial release mechanism, these include the magnetic connection of the SEP source to the observer (Rouillard et al., 2011; Lario et al., 2014; Kouloumvakos et al., 2022), particle acceleration in interplanetary shocks driven by coronal mass ejections (e.g. Reames, 2013), shock evolution and geometry (Tylka et al., 2005), extended SEP injections from propagating CME-driven shocks (e.g. Lario et al., 2016), existence of seed populations (Desai et al., 2006), convection by the solar wind (Desai and Giacalone, 2016), pitch-angle scattering, adiabatic deceleration and drifting in the interplanetary magnetic field (Dröge, 2000; Dröge et al., 2010; Dalla et al., 2015), cross-field diffusion (e.g. Giacalone and Jokipii, 1999; Giacalone and Jokipii, 2012, and references therein), and reflection of particles from propagating barriers beyond 1 AU (Bieber et al., 2002). To highlight an instructive example, a considerable amount of work has been done recently on numerical simulation of SEP acceleration by CME-driven shocks in the solar corona (Kozarev et al., 2013; Kong et al., 2017; Kong et al., 2019; Kozarev et al., 2022); the results underscore the important role played by the structure of the coronal magnetic field in the early stages of an unfolding SEP event. Depending on the species and energy range of the studied SEPs and the longitudinal and radial separation of the observer from the particle source, a single event may display markedly different maximum intensities and profile shapes (e.g. Lario et al., 2013; Paassilta et al., 2018).

Extensive modelling works have been put forth with respect to most of the above processes, aiming at either disentangling the physics at work (e.g. Wijsen et al., 2019; van den Berg et al., 2020) or at providing usable space weather predictions (Pomoell et al., 2015). Our work directly addresses both through a simple and straightforward approach, which is to have a standard parametric description of the entire SEP time profile at a given energy, from the onset to the peak and the decay phase, and to cross-compare the obtained fit parameters to quantities of interest.

Kahler and Ling (2017) showed that a particular analytical function form, a modified Weibull function, is well suited to describe the intensity profile of a typical SEP event that features a high peak intensity and significant increases over a wide range of particle energies. Fitting this type of function to the recorded intensities allows one to parametrise the event with a small number of numerical values that easily lend themselves to in-depth investigation, e.g. for correlations between the function parameters and observable solar quantities such as the longitude and magnitude of the event-related X-ray flare. This has the potential to lead to new discoveries about the details of SEP release and acceleration. More directly, such an approach could prove valuable in predicting space weather based on solar observations. Since a complete theoretical picture of the processes involved is very challenging to attain, even workable empirical models of their combined effects are an attractive prospect. There is thus a decided interest to apply the aforementioned parametrisation to a large and diverse group of SEP events, so as to expand the scope of the study carried out by Kahler and Ling (2017) and, through improved statistics, to gain a better understanding of the phenomena that bear on event intensity profiles.

In this paper, we investigate a group of 86 SEP events with iron enhancements listed by Raukunen et al. (2016) by fitting a form of modified Weibull function to their proton intensity profiles at 18.2 MeV (where possible). We additionally rely on information from Barcewicz (2019), who carried out an extensive analysis of these events and employed a potential field source surface (PFSS) -based modelling of magnetic field lines in the solar corona (Altschuler and Newkirk, 1969). The latter work yielded three characteristic angles related to the magnetic connection between the associated solar flare of the SEP event and the observer during the initial phase of each event. Our main emphasis lies on attempting to identify systematic dependencies, if any, between the event intensity profile shapes as described by the fit parameters and the characteristics of the events (most importantly magnetic connectivity and iron-to-carbon ratio), as well as further exploring the method proposed by Kahler and Ling (2017) in practice.

This article is structured in the following fashion. In Section 2, we discuss the data set and the mathematical approaches used in our work; in Section 3, we present a list of 25 SEP events for which we obtained successful function fits and study the distributions of the fit parameters, as well as the dependencies between the parameters and several other quantities of interest. Finally, we discuss the results and outline our conclusions in Section 4. The details of the function fitting process are explained in Appendix A, the connection angle (i.e. the longitudinal distance between the X-ray flare associated with the event and the Parker spiral footpoint connecting the Sun and the observer) as an alternate measure of magnetic connectivity is briefly discussed in Appendix B, and Appendix C contains a brief description of a comparison made between two energetic solar proton intensity data sets, made in an effort to ensure that the choice of data set does not compromise our results and conclusions.

2. Data and methods

The proton intensity data used in our analysis was drawn from the second version of the Reference Data Set (RDS) of Solar Energetic Particle Environment Modeling (SEPEM) (Crosby et al., 2015). RDS provides proton differential fluxes for the years 1973—2015 at eleven proton energy values and has been generated through cross-calibration (Sandberg et al., 2014), energy re-binning and merging of Geostationary Operational Environmental Satellite (GOES) and the earlier Synchronous Meteorological Satellite (SMS) proton flux datasets. The data, natively available at 5-min time resolution, were averaged to 15-min

bins to eliminate excessive intensity fluctuations. Newer versions of the reference data set are currently available, but they were not used due to the fact that the background intensity has been subtracted in them, which was considered to complicate the function fitting process (for example, by potentially obscuring the onset of a very slowly rising event) without providing a commensurate benefit for the analysis. Even though e.g. Solar and Heliospheric Observatory/Energetic and Relativistic Nuclei and Electron (SOHO/ERNE; Torsti et al., 1995) proton data offer a generally lower background intensity and better measurement statistics compared to RDS, as well as the possibility to obtain error estimates for the measured intensities directly via particle counts, we chose RDS over ERNE data due to the absence of data gaps in the former. To guarantee that this selection does not have a serious effect on our results and conclusions, we performed a comparison between ERNE and RDS data; for a summary, see Appendix C.

Kahler and Ling (2017) studied the time-intensity profiles of about a dozen large solar proton events and demonstrated that a modified Weibull function models the observations well (see also Laurenza et al., 2015). Based on this earlier treatment, we define the fit function as follows:

$$F(t) = \begin{cases} A_0\left(\frac{t-t_0}{b}\right)^{a-1} \exp\left(-\left(\frac{t-t_0}{b}\right)^{a}\right) + F_{\mathrm{bg}}; t > t_0 \\ F_{\mathrm{bg}}; t \leqslant t_0 \end{cases}. \quad (1)$$

Here, t is time (measured in hours), A_0 is a scaling parameter corresponding to the maximum intensity of the event, and a and b control the overall shape of the intensity enhancement and the duration of the event, respectively;[1] t_0 is the notional delay between the time axis origin and the proton event onset. F_{bg} is the pre-event background intensity. In a physically meaningful case, A_0 and b are always greater than zero, while a is less than zero. The time axis was defined so that the onset of the event-related soft X-ray flare corresponds to $t = 0$, and the onset shift parameter t_0 was restricted to values greater than -2.0 h.

We can write A_0 in terms of peak intensity by taking the derivative of the function defined in Eq. 1, which must satisfy the condition $\mathrm{d}F(t)/\mathrm{d}t = 0$ at the time of the maximum detected intensity during the event. If we then also introduce the term I_0, which is the modelled peak intensity in physical units, A_0 can be expressed as

$$A_0 = I_0\left(\frac{a-1}{a}\right)^{\frac{1-a}{a}} \exp\left(\frac{a-1}{a}\right). \quad (2)$$

For the purposes of detailed study of the intensity profiles, we additionally define the rise time of the profile (i.e. the time required to reach the maximum intensity after starting from the pre-event background), τ_{rise}, as

$$\tau_{\mathrm{rise}} = b\left(1 - \frac{1}{a}\right)^{\frac{1}{a}}, \quad (3)$$

and the total time modelled to elapse between the flare onset ($t = 0$) and the intensity maximum, $t_{\max}$, as

$$t_{\max} = t_0 + \tau_{\mathrm{rise}}. \quad (4)$$

It should be noted that neither τ_{rise} nor $t_{\max}$ involves an explicit onset criterion for the modelled intensity profile, such as might be used with observed intensity data; as far as these measures are concerned, the event is considered to have commenced as soon as $F(t) > F_{\mathrm{bg}}$.

Fig. 1 demonstrates the shape of the modified Weibull function as defined in Eqs. 1 and 2. The function is shown plotted for a range of values of a and b so that in the top panel, a is given six different values between -0.3 and -3.0 while b remains fixed at 10 h, whereas in the bottom panel, b is similarly varied between 2.0 h and 30.0 h and a is fixed at -1.0. For the sake of clarity, the other three parameters are kept constant in all cases ($t_0 = 0$ h, $I_0 = 1.0$, and $F_{\mathrm{bg}} = 0.01$). In particular, it can be clearly seen that when a approaches zero (its absolute value decreases), the rise and peak phase become very brief and sharp. b determines the time scale, with an increase in its value corresponding with lengthening of the intensity profile.

When studying the events in practice, we typically did not consider the entire time range of the event but limited the time range of interest between $t = -5.0$ h and either the event end as given in literature, the onset of the next notable intensity rise, or until a reasonable point where the intensity was considered to have declined substantially after the maximum. A more detailed description of the fitting process is provided in Appendix A.

Fig. 2 shows four representative, successful fits to different types of events; the event numbers refer to Table 1 (see the following section). Included are event 1 (large Fe/C ratio, $t_0 < 0$, small b); event 12 (large Fe/C ratio, $t_0 > 0$, large b); event 8 (nominal Fe/C ratio, $t_0 > 0$, large b); and event 16 (nominal Fe/C ratio, $t_0 < 0$, small b). The upper panels show the detected proton intensities (in red) and the fit curve (in blue) in normalized units, while the lower panels show the simultaneous GOES X-ray observations.

After the fit parameters were obtained for all events that could be successfully fitted, we constructed cumulative probability distributions for the fit parameters using a Monte Carlo-based approach that takes into account the statistical uncertainties of the parameters. Using the error estimates for the fit parameters and adding a pseudo-random, normally distributed constant to every data point, we generated a family of 10001 simulated cumulative distribution functions. When the individual data points are re-ordered by their magnitude, the 5001st (middle) curve can be considered to represent the median value, while the 1587th and 8413th curve similarly correspond to the $-1\ \sigma$ and $+1\ \sigma$ error bounds, respectively, of the simulated curve family.

[1] In Kahler and Ling (2017), Greek letters α and β are used instead of a and b. Latin letters were substituted here to avoid confusion with the magnetic field parameters α and β.

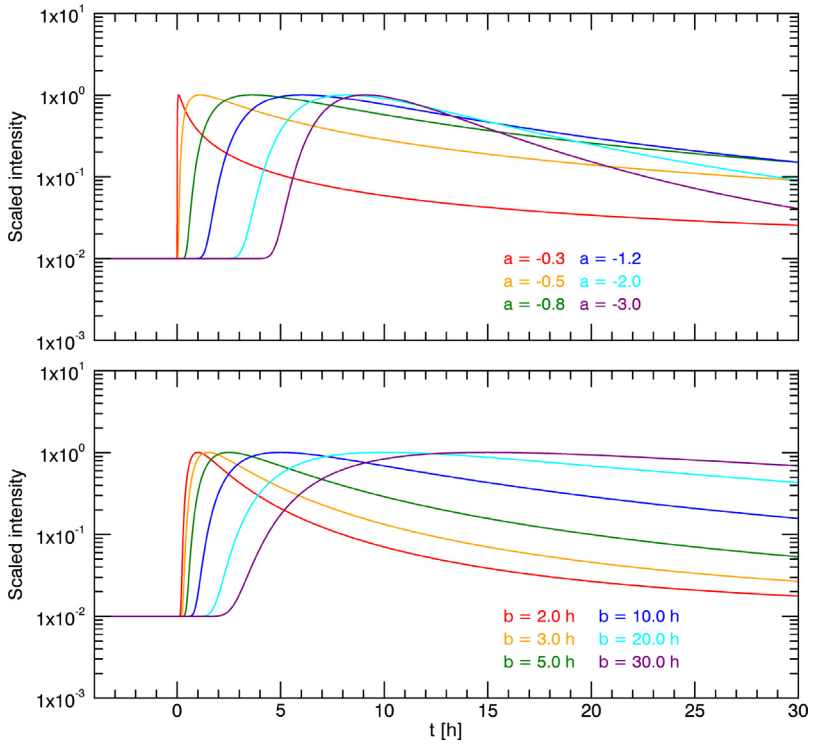

Fig. 1. Families of modified Weibull functions, modelling scaled particle intensity as a function of time. Top panel shows six cases of a values, with b fixed at 10.0 h; bottom panel shows six cases of b values, with a fixed at −1.0. For all curves, $t_0 = 0$ h, $I_0 = 1.0$, and $F_{bg} = 0.01$. These correspond to τ_{rise} values of 0.0754 h, 1.11 h, 3.63 h, 6.03 h, 8.16 h, and 9.09 (the top panel) and 1.00 h, 1.50 h, 2.50 h, 5.00 h, 10.0 h, and 15.0 h (the bottom panel), respectively. Note that the ordinate is logarithmic.

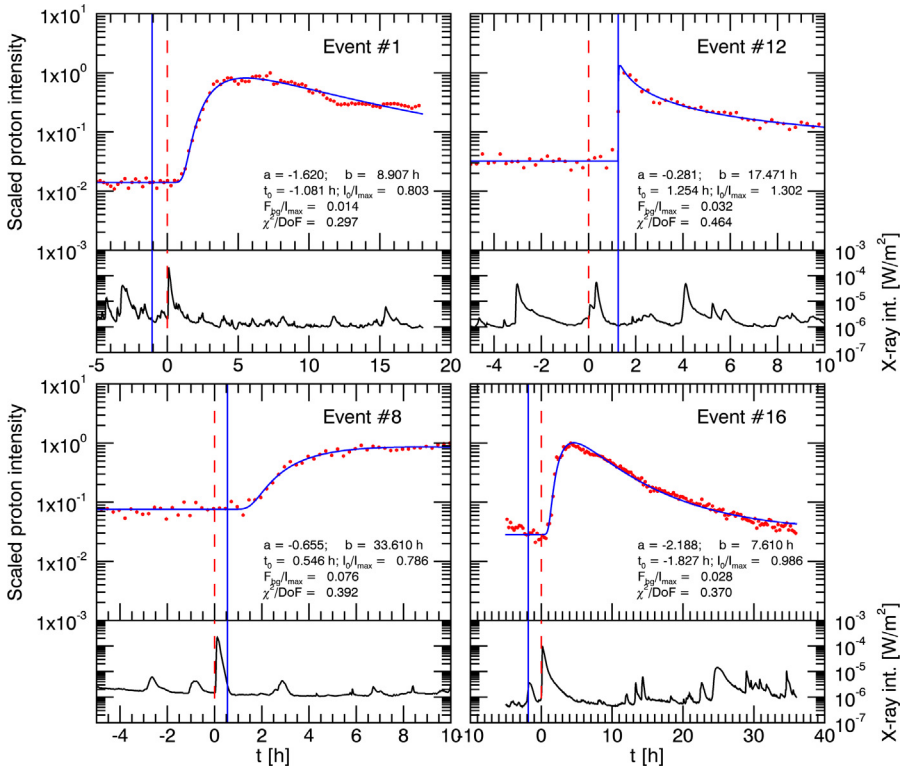

Fig. 2. The curve fits to events 1, 12, 8, and 16 (from left to right and top down). The measured proton intensity is in red, the fit curve in blue (in the upper panels), and the concurrent GOES soft X-ray intensity in black (in the lower panels). The solid vertical blue line denotes the value of the t_0 parameter, and the dashed vertical red line the time of onset of the event-related flare, i.e. the time axis origin.

Table 1
The onset date, associated solar X-ray flare latitude and longitude, data selection length, fit function parameters, iron-to-carbon ratio, and modelled magnetic field (MF) parameters for the studied events (note: 1 pfu = 1 particle cm^{-2} s^{-1} sr^{-1}).

Event					Function fit									MF parameters		
#	Date of onset	θ	ϕ [°]	Fe/C	L [h]	$-a$	b [h]	t_0 [h]	I_0 [pfu/MeV]	F_{bg} [pfu/MeV]	τ_{rise} [h]	t_{max} [h]	χ^2/DoF	α [°]	β [°]	λ [°]
1	1997-Nov-04	S14	33	0.98±0.09	18	1.62±0.24	8.91±0.40	−1.08±0.58	$(1.53\pm0.36)\times10^{0}$	$(2.66\pm0.13)\times10^{-2}$	6.62±0.47	5.54±0.75	0.30	77.4	3.0	0.8
2	1997-Nov-06	S18	63	1.12±0.04	11	0.74±0.32	41.25±43.50	−0.59±0.82	$(1.09\pm0.30)\times10^{1}$	$(7.37\pm0.38)\times10^{-2}$	1.74±14.21	2.64±14.23	0.25	72.7	0.7	1.2
3	1998-May-02	S15	15	2.00±0.30	36	0.79±0.05	8.67±0.50	0.10±0.09	$(3.11\pm0.71)\times10^{0}$	$(2.39\pm0.13)\times10^{-2}$	3.05±0.20	3.16±0.22	0.61	38.0	2.0	6.6
4	1998-May-06	S11	65	0.86±0.09	36	0.88±0.04	2.75±0.13	0.42±0.04	$(5.26\pm1.22)\times10^{0}$	$(2.97\pm0.16)\times10^{-2}$	1.16±0.06	1.58±0.07	0.53	48.6	5.5	2.2
5	2000-Jun-10	N22	40	1.54±0.31	36	1.05±0.05	5.71±0.19	0.33±0.10	$(1.52\pm0.35)\times10^{0}$	$(1.32\pm0.07)\times10^{-2}$	3.02±0.12	3.35±0.16	0.45	15.3	21.8	24.2
6	2000-Jun-18	N20	85	0.26±0.14	12	1.18±0.31	4.05±0.38	0.36±0.45	$(7.12\pm1.68)\times10^{-2}$	$(1.60\pm0.08)\times10^{-2}$	2.40±0.37	2.76±0.58	0.38	46.5	12.9	13.5
7	2000-Jun-23	N23	72	1.25±0.70	12	1.32±0.49	2.66±0.44	0.90±0.52	$(3.10\pm0.78)\times10^{-2}$	$(1.34\pm0.06)\times10^{-2}$	1.74±0.40	2.64±0.65	0.48	39.9	5.2	8.6
8	2000-Nov-24	N22	3	0.20±0.01	10	0.66±0.44	33.61±58.58	0.55±1.04	$(2.03\pm0.49)\times10^{-1}$	$(1.97\pm0.10)\times10^{-2}$	8.17±14.61	8.71±14.65	0.39	38.1	69.3	29.5
9	2001-Mar-29	N16	12	0.54±0.05	30	1.09±0.20	30.82±4.72	−1.36±1.12	$(7.98\pm1.80)\times10^{-1}$	$(1.39\pm0.07)\times10^{-2}$	16.97±3.00	15.61±3.20	0.21	20.1	30.4	21.6
10	2001-Apr-15	S20	84	0.52±0.02	36	1.83±0.09	9.24±0.27	−1.91±0.24	$(2.77\pm0.63)\times10^{1}$	$(2.70\pm0.14)\times10^{-2}$	7.28±0.25	5.37±0.34	0.82	34.9	58.3	27.3
11	2001-Oct-22	S18	−18	0.41±0.10	36	0.83±0.10	22.48±2.93	0.57±0.44	$(2.63\pm0.60)\times10^{-1}$	$(1.47\pm0.07)\times10^{-2}$	8.70±1.26	9.27±1.34	0.85	54.7	39.9	39.2
12	2002-Feb-20	N12	72	1.27±0.20	10	0.28±0.12	17.47±32.88	1.25±0.01	$(5.74\pm3.68)\times10^{-1}$	$(1.42\pm0.07)\times10^{-2}$	0.08±0.15	1.33±0.15	0.46	27.7	3.6	8.2
13	2002-Aug-18	S12	19	4.35±0.42	11	1.73±0.84	5.95±1.09	−0.31±1.57	$(7.16\pm1.73)\times10^{-2}$	$(2.14\pm0.10)\times10^{-2}$	4.57±1.16	4.27±1.95	0.58	11.0	29.1	25.2
14	2002-Aug-20	S10	38	7.05±0.50	18	1.32±0.45	3.23±0.52	0.41±0.58	$(4.58\pm1.13)\times10^{-2}$	$(2.13\pm0.10)\times10^{-2}$	2.11±0.46	2.51±0.74	0.34	N/A	27.7	N/A
15	2002-Aug-22	S07	62	2.29±0.36	28	1.08±0.10	10.60±0.51	−0.05±0.26	$(9.01\pm2.05)\times10^{-1}$	$(1.48\pm0.08)\times10^{-2}$	5.75±0.37	5.70±0.46	0.64	33.0	4.0	9.9
16	2003-May-31	S07	65	0.34±0.09	36	2.19±0.17	7.61±0.50	−1.83±0.44	$(7.52\pm1.71)\times10^{-1}$	$(2.16\pm0.11)\times10^{-2}$	6.41±0.45	4.58±0.63	0.37	N/A	40.5	N/A
17	2006-Dec-13	S06	23	1.06±0.03	21	1.46±0.18	11.58±0.41	−1.67±0.53	$(2.09\pm0.48)\times10^{1}$	$(1.89\pm0.10)\times10^{-1}$	8.08±0.50	6.42±0.73	0.23	48.0	5.4	0.1
18	2006-Dec-14	S07	46	0.90±0.22	21	1.71±0.27	1.91±0.22	1.65±0.20	$(5.80\pm1.39)\times10^{0}$	$(4.35\pm0.19)\times10^{-1}$	1.46±0.19	3.11±0.27	0.90	50.8	0.5	2.7
19	2011-Jun-07	S21	54	0.60±0.11	10	1.12±0.51	10.23±3.17	−0.32±1.08	$(1.33\pm0.32)\times10^{0}$	$(1.13\pm0.06)\times10^{-1}$	5.81±2.18	5.49±2.44	0.17	N/A	34.6	N/A
20	2011-Aug-04	N19	36	0.46±0.02	15	1.53±0.35	12.77±0.80	−1.84±0.96	$(2.90\pm0.67)\times10^{0}$	$(2.94\pm0.15)\times10^{-2}$	9.20±1.01	7.36±1.39	0.55	25.6	28.0	34.0
21	2011-Aug-09	N17	69	0.69±0.15	36	1.41±0.10	5.61±0.28	−0.82±0.22	$(9.95\pm2.26)\times10^{-1}$	$(3.34\pm0.17)\times10^{-2}$	3.84±0.22	3.03±0.31	0.45	N/A	41.4	N/A
22	2012-Mar-13	N19	59	0.23±0.02	36	1.20±0.07	5.52±0.21	0.22±0.15	$(1.58\pm0.36)\times10^{1}$	$(2.91\pm0.14)\times10^{-1}$	3.33±0.16	3.55±0.22	0.47	61.9	7.2	0.7
23	2012-Sep-28	N06	37	0.57±0.15	36	0.95±0.08	9.89±0.52	0.75±0.22	$(5.81\pm1.32)\times10^{-1}$	$(2.57\pm0.12)\times10^{-2}$	4.61±0.31	5.36±0.38	0.21	30.1	43.9	18.1
24	2013-Apr-11	N09	−12	0.96±0.13	14	1.39±0.48	18.66±3.97	−1.59±1.50	$(3.19\pm0.73)\times10^{0}$	$(1.76\pm0.09)\times10^{-2}$	12.62±3.25	11.02±3.57	0.52	41.9	72.6	55.7
25	2014-Apr-18	S20	34	0.29±0.03	31	0.76±0.09	35.58±7.48	−0.29±0.37	$(1.45\pm0.33)\times10^{0}$	$(1.61\pm0.08)\times10^{-2}$	11.86±2.62	11.57±2.64	0.74	66.7	6.1	0.3

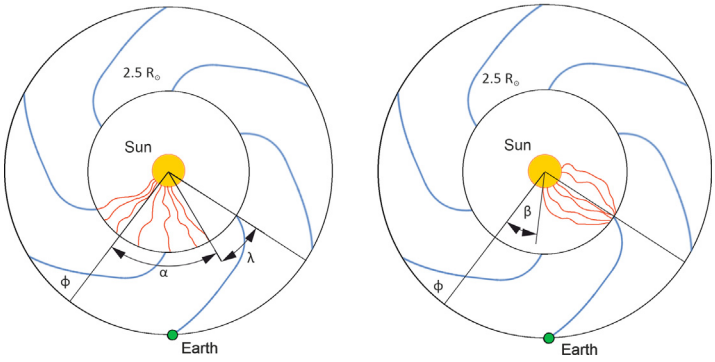

Fig. 3. A schematic representation of the heliospheric magnetic field in the PFSS model and the magnetic connection parameters α, β, and λ. The modelled magnetic field lines are drawn in red and the Parker spiral in blue; ϕ denotes the solar longitude of the event-related X-ray flare. In the left-hand image, the field lines are traced upwards from the flare site; in the right-hand image, they are traced downwards from the source surface. Note that α, β, and λ include the latitudinal as well as longitudinal distance. The elements are not to scale.

3. Results

This work employs the event listing given in Raukunen et al. (2016). The magnetic connection between the particle source and the observer in these events was studied in Barcewicz (2019), where the connection is characterized with three angular parameters, α, β, and λ. These parameters were calculated through a PFSS-based modelling of the magnetic field present in the solar corona (Altschuler and Newkirk, 1969; Schrijver and De Rosa, 2003).

Fig. 3 illustrates the relationships between the angle parameters, the event-associated flare, the nominal Parker spiral, and the modelled magnetic field lines. The inner black circle represents the source surface at 2.5 $R_\odot$, the Parker spiral is drawn in blue, and modelled field lines are drawn in red. ϕ is the flare longitude. In the left-hand image, the field lines are traced upwards from the flare location; α denotes the largest angular distance between a field line endpoint on the source surface and the event-related flare, and λ is the angular distance between the nominal Parker spiral footpoint and the endpoint of the nearest modelled field line on the source surface. In the right-hand image, the red field lines are traced from the source surface downwards; β is the smallest angular distance between the flare and the heliospheric field lines connected to the particle source. All three of these parameters, α, β, and λ, are measured over both the longitudinal and the latitudinal components of the distance.

We initially considered the 86 events present on the list at one energy channel in the deka-MeV range, 18.2 MeV. This energy channel was chosen primarily due to its relevance to space weather and also because it offers a good compromise from the viewpoint of statistics: a number of the events listed in Raukunen et al. (2016) and comparable works might not be clearly discernible at considerably higher proton energies, whereas at lower energies, closely spaced, relatively small events in particular may be obscured by the often slow decay of the SEP intensity after the event maximum. However, 20 of the 86 listed events (23%) are effectively unanalysable in this context because of insufficient information about the event-related solar X-ray flare, doubtful flare identification, or brief duration (less than 10 h) of the event itself. Furthermore, a considerable proportion of the events feature very small intensity increases over the pre-event background (27 cases, 31%), or the intensity enhancement occurs in multiple successive stages (7 cases, 8%), making them difficult and physically questionable to model with a simple function such as that defined in Eq. 1. A function fit was attempted for each of the remaining 32 events (37%). The nominally successful cases where the χ^2 value of the fit,[2] divided by the degrees of freedom (DoF), was equal to ≈ 1.0 or less were inspected visually. Physically doubtful fits, i.e. the cases where the onset of the event was not satisfactorily modelled (7 cases, 8%), were discarded at this stage. After the final round of elimination, 25 well-fitted events (29%) remained, and these were selected for detailed study.

The main characteristics of the studied events are presented in Table 1. Included are the date of onset of the SEP event, solar latitude and longitude of the associated soft X-ray flare (θ and ϕ, in degrees), the detected iron-to-carbon ratio (Fe/C) averaged over the event, the duration of the intensity data chosen to be fitted (L; in hours, counted onwards from the onset of the event-related flare), fit function parameters and related quantities ($a, b, t_0, I_0, F_{\mathrm{bg}}, \tau_{\mathrm{rise}}, t_{\max}$, and the goodness-of-fit statistic χ^2/DoF), and the solar magnetic field parameters (α, β, λ; in degrees). Positive and negative longitude values refer to western and eastern solar longitudes, and "N" and "S" indicate northern and southern latitudes, respectively. All dates are UT. 1-sigma statistical error limits are given for those tabulated quantities for which they are available. Event date of onset, flare position, and the Fe/C ratio are taken from Raukunen et al. (2016), and the magnetic field parameters from Barcewicz (2019).

[2] Note well that here and in the following, χ^2 refers to the fit to the logarithmic normalized intensities, not actual intensities in physical units!

It was felt desirable to obtain additional insight into the fitting process itself before proceeding with a statistical analysis of its results *vis-à-vis* the magnetic field parameters, and to this end, we briefly studied the curve fitting parameters—a, b, and the ratio I_0/F_{bg} on one hand and t_0 on the other—for internal dependencies. Fig. 4 shows t_0 plotted as a function of a and b, and additionally I_0/F_{bg} as a function of t_0.

There are indeed indications that such dependencies exist: although prominent scatter and fairly large statistical uncertainties make firm conclusions somewhat difficult to reach, a correlation between a and t_0 seems plausible, and conceivable between b and t_0. Another likely correlation exists between t_0 and I_0/F_{bg}; large values of the latter, i.e. events which feature large maximum intensities in relation to the pre-event background, tend to be associated with small values of t_0, and vice versa. As t_0 thus cannot be said to be truly independent of all the other fit parameters, it should not be regarded as directly representing the physical delay of the proton intensity rise after the onset of the event-related X-ray flare. Instead, t_0 apparently interacts in a non-trivial manner with the other parameters in determining the shape of the fit curve.

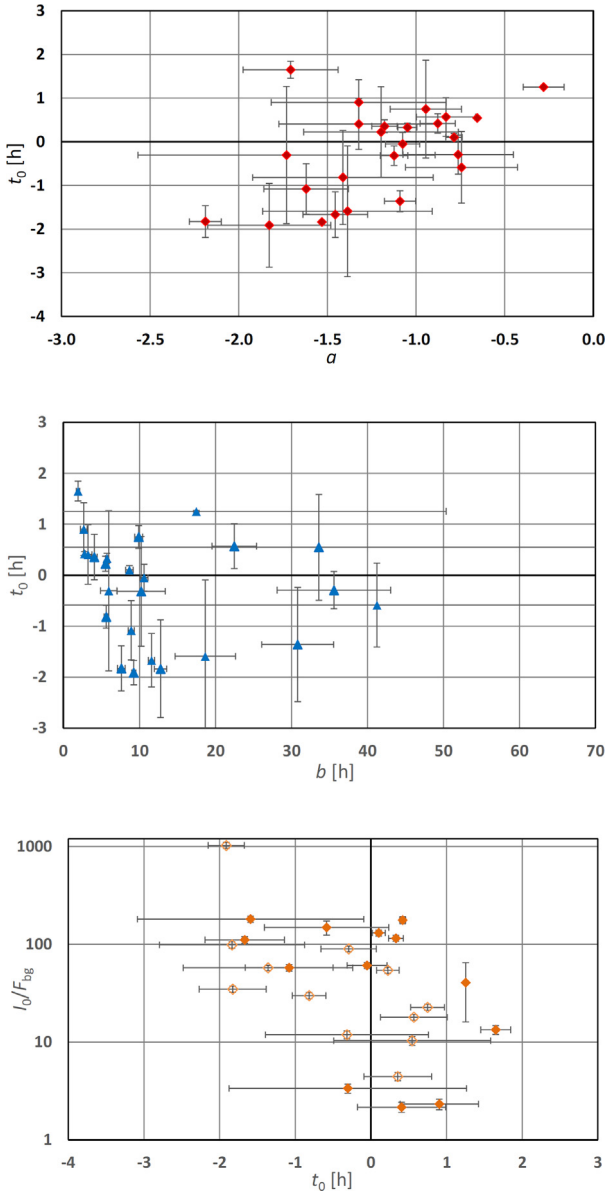

Fig. 4. Selected function fit parameters for the studied events, plotted against one another. Top panel: t_0 (in hours) versus a; middle panel: t_0 (in hours) versus b (in hours); bottom panel: the ratio of I_0 and F_{bg} versus t_0 (in hours). The vertical and horizontal bars denote the statistical 1-σ errors. In the bottom panel, filled symbols represent events with a high Fe/C ratio ($\geqslant 0.8$), while hollow symbols represent events with nominal Fe/C ratio (< 0.8).

So as to be able to determine whether the relative heavy ion abundance of the events, in addition to and together with their magnetic connectivity, has a discernible effect on their time-intensity profiles, we divided the events into two categories so that cases with an Fe/C ratio of $\geqslant 0.8$ are considered iron-rich and the rest nominal with respect to ion abundances. Unless stated otherwise, these categories are denoted in all of the following figures with solid and hollow symbols, respectively. The value of 0.8 was chosen because it ensures that the two groups are almost equal in size, facilitating comparisons between them. For this reason and owing to the fact that the event list selected as the basis of our study is focussed on iron-rich cases (in a bid to ensure that such events, which tend to rise and fall fairly sharply, are well represented in our sample; see also the discussion in Section 4), it exceeds the coronal and slow solar wind value of Fe/C by a factor of $\approx$ 2–3 (see e.g. Reames, 2019, and references therein).

As the first step in our effort to gain a quantitative understanding of how the magnetic connection of the particle source to the observer shapes the time-intensity profile of the event and how this relationship might vary with the detected relative abundances of heavy ion species, we briefly considered a and b as functions of the solar longitude of the event-related flare. These are shown in Fig. 5 (panels a and b). In the case of a, there is prominent scatter and no obvious correlation. However, a faint linear or quadratic dependence on the flare longitude could conceivably exist for b, especially if the events with very large statistical errors are disregarded as dubious results. The smallest b values fall within the solar longitude range where a reasonably good magnetic connection to the observer might be expected (between about 45 and 70 degrees west). In particular for a, a conspicuous and consistent differentiation between iron-rich and nominal-abundance events is absent, but the nominal-abundance events might display a tendency for larger b values than do iron-rich events.

For events 2, 8, and 12, the relative statistical uncertainty (1-sigma error) of b is >100%. As a result, they were rejected from the subsequent stages of our analysis.

Utilizing the results of the PFSS-based modelling presented by Barcewicz (2019), we next investigated the relationships between fit parameters a and b and the magnetic field parameters α, β, and λ. It seems evident that

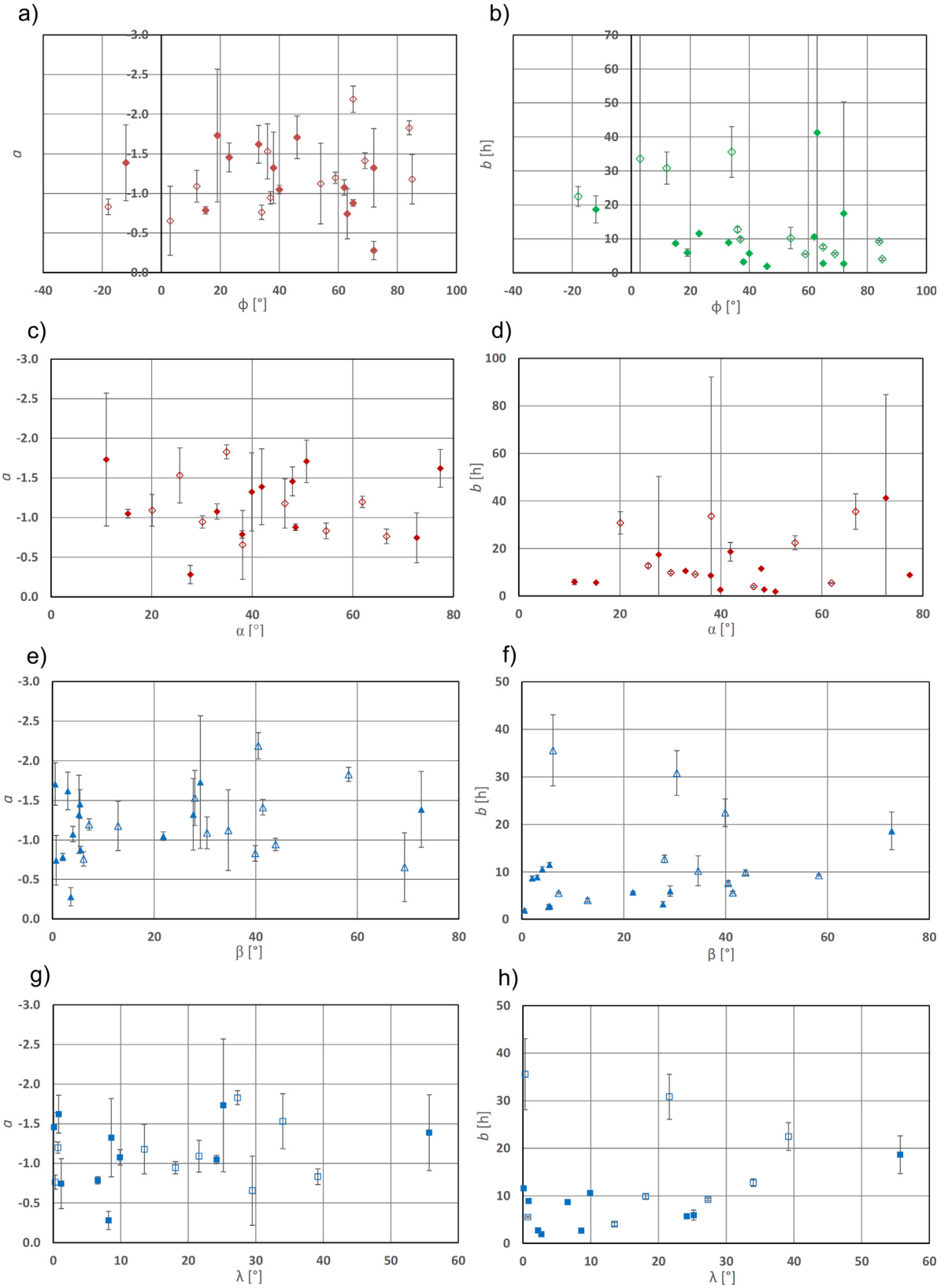

Fig. 5. Function fit parameters a and b (the latter in hours) plotted against the solar longitude of the event-related flare ϕ (in degrees) and the magnetic angles α, β, and λ (in degrees) for the studied events. From left to right and top down: ϕ versus a (panel a), ϕ versus b (panel b), a versus α (panel c), b versus α (panel d), a versus β (panel e), b versus β (panel f), a versus λ (panel g), and b versus λ (panel h). Filled symbols represent events with a high Fe/C ratio ($\geqslant 0.8$), while hollow symbols represent events with nominal Fe/C ratio (< 0.8). The vertical bars denote the statistical 1-σ errors. Events 2, 8, and 12 feature excessive uncertainties with respect to b and are not shown in panels f and h.

no substantial correlations exist between α and either a or b (Fig. 5, panels c and d). Likewise, there is only a very slight (anti-) correlation at the most between a and β, as well as between a and λ (Fig. 5, panels e and g). In contrast, b would appear to exhibit evidence of a positive correlation with respect to both β and λ (Fig. 5, panels f and h); nevertheless, the exact type (linear, quadratic, or other) of this dependence is difficult to determine with confidence due to scatter and the limited number of the data points. It is also noteworthy that the groups of iron-rich and nominal-abundance events are not strongly differentiated from one another in this context.

Fig. 6 shows the event rise time τ_{rise} (Eq. 3) and and the time delay between flare onset and the event intensity peak, t_{max} (Eq. 4), plotted against α, β, and λ. Even though neither τ_{rise} nor t_{max} displays a clear correlation with α (Fig. 6, panels a and b), it appears fairly likely that—leaving aside two nominal-abundance cases with relatively large statistical uncertainties—a positive correlation exists between τ_{rise} and both β and λ (Fig. 6, panels c and e), as

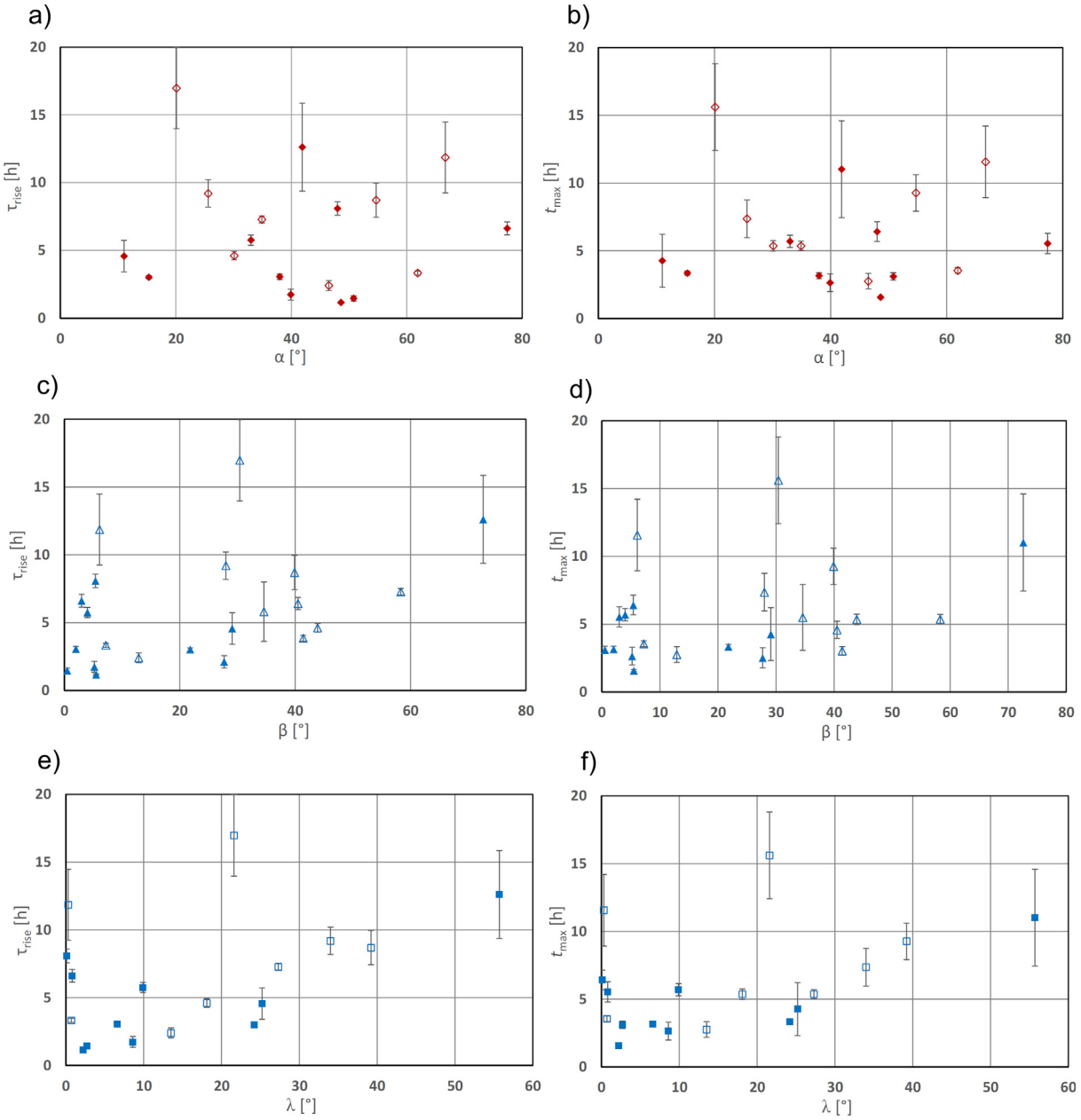

Fig. 6. The modelled event rise time τ_{rise} (in hours) and the delay between the onset of the event-related flare and the modelled event intensity peak, t_{max} (in hours), plotted against the magnetic angles α, β, and λ (in degrees) for the studied events. From left to right and top down: τ_{rise} versus α (panel a), t_{max} versus α (panel b), τ_{rise} versus β (panel c), t_{max} versus β (panel d), τ_{rise} versus λ (panel e), and t_{max} versus λ (panel f). Filled symbols represent events with a high Fe/C ratio ($\geqslant 0.8$), while hollow symbols represent events with nominal Fe/C ratio (< 0.8). The vertical bars denote the statistical 1-σ errors. Events 2, 8, and 12, which feature excessive uncertainties with respect to b (and therefore τ_{rise} and t_{max}), are not shown.

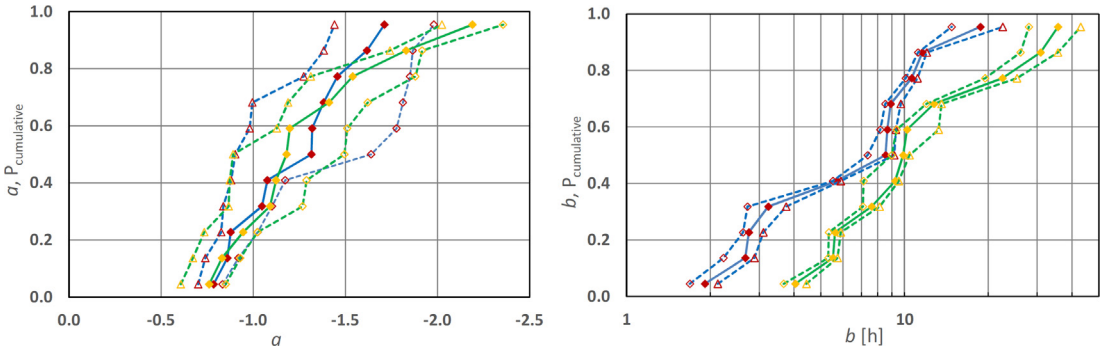

Fig. 7. Monte Carlo-derived cumulative probability distributions for iron-rich (red symbols) and nominal-abundance (yellow symbols) events. The fit parameter a is shown in the left-hand panel, b in the right-hand panel (note that the abscissa of the latter is logarithmic). The solid lines and symbols denote the median values, while and the dashed lines and hollow symbols denote the $-1\ \sigma$ and $+1\ \sigma$ bounds of each distribution. Events 2, 8, and 12 are excluded; see text for details.

well as between $t_{\max}$ and β and λ (Fig. 6, panels d and f). For these quantities, there is considerable similarity to the behaviour of b as a function of the magnetic connectivity angles. The precise type of this correlation is uncertain due to the statistical limitations, as with b, but at least linear or quadratic models again seem plausible. No prominent separation of iron-rich and nominal-abundance events can be seen.

In a bid to investigate further whether the iron-rich and nominal-abundance event populations actually differ from each other with respect to a and b, we recast the populations in terms of cumulative probability distributions. Within both iron-rich and nominal-abundance groups, each event was assigned a value $P_{\text{cumulative}}(i)$, defined as follows:

$$P_{\text{cumulative}}(i) = \frac{i - 0.5}{N}, \tag{5}$$

where i is the rank of the data point when the points are ordered from smallest to largest according to the absolute value of the fit parameter of interest and N is the total number of data points in the group. To take into account the statistical uncertainties present in the fit parameters, we then applied a Monte Carlo-based analysis (see Section 2) to the cumulative distributions.

The results are presented as Fig. 7. In the case of the a distributions (Fig. 7, the left-hand panel), the overlap in the two populations is extensive, making it rather unlikely that the differences between iron-rich and nominal-abundance events are statistically meaningful in this respect. Conversely, the b distributions (Fig. 7, the right-hand panel) are distinct almost everywhere and diverge markedly both before and after about $0.5 < P_{\text{cumulative}} < 0.6$. This suggests that high b values are significantly less common for iron-rich events than for events with nominal ion species abundances.

Based on an intuitive understanding, we might expect the absolute value of a to be small for small values of β and λ, indicating a profile with a rapid intensity rise from the background level and a momentary, well-defined maximum. An increase in β and λ (a weaker connection) would then, in general, cause the absolute value of a to increase likewise (i.e., the rise becomes more gradual)[3] due to the SEPs being subjected to a greater amount of scattering since they must spread across more magnetic field lines in order to reach the observer. However, this notion is too simplistic in light of the evidence: even nominally well-connected events that only involve a single intensity rise display a variety of possible profile shapes at the Earth. We have not attempted to take into account the details of the particle acceleration and transport processes occurring in each individual case (such as delayed shock buildup en route, multiple merging particle injections when these are not easily distinguishable on visual inspection of the event intensity plots, etc.); further investigation into these and a more comprehensive modelling might allow us to gain a better insight into the issue. Finally, while we cannot definitively rule out the possibility that the characteristics of the curve fitting process itself—which is sensitive to fluctuations and errors in the data near the event onset—play some role in blurring a putative correlation between a and the magnetic angles or the Fe/C ratio, such an explanation can hardly account for all aspects of the behaviour of a.

Conversely, b in fact appears to behave as a function of ϕ, β, and λ much in the fashion that the basic model outlined above would predict the absolute value of a to do, apart from a handful of outlying cases. A closely comparable situation also exists with respect to the event rise time measures τ_{rise} and $t_{\max}$ as functions of β and λ.

4. Discussion and conclusions

We considered a total of 86 SEP events that occurred between 1997 and 2014 with respect to their time-intensity profiles. Making use of the SEPEM RDS dataset, we fitted a modified Weibull function to the measured pro-

[3] Since the time scaling also has an effect on the absolute shape of the rise portion of the curve, this interpretation assumes no drastic changes in b.

ton intensities at 18.2 MeV in order to be able to characterise the profiles with five numerical parameters. We then studied these parameters for dependencies and correlations with respect to the solar longitude of the event-related X-ray flare, three angles describing the magnetic connection between the particle source and the observer, and the iron-to-carbon ratio of the events. After discarding the events for which the available information concerning the quantities mentioned above was incomplete or doubtful, together with cases where our function fitting method failed to produce a reasonable fit for any reason, 25 events (29%; see Table 1) remained for a detailed analysis. The primary causes for rejection were very low maximum intensity or brief duration of an event, multiple overlapping intensity enhancements, and missing or possibly incorrect flare information.

Although the fairly small size of the useful event sample compelled us to work with rather limited statistics, the following three main conclusions seem warranted.

(i) The fit parameter primarily controlling the shape of the rise and peak of the intensity profile, a, does not show a recognizable correlation with flare longitude ϕ, and it is at most weakly dependent on the magnetic angles β and λ. Furthermore, there is no substantial difference in the distribution of a values for iron-rich (Fe/C $>$ 0.8) and nominal-abundance (Fe/C $\leqslant$0.8) events. Taken together, these observations indicate that if all other conditions are equal, the intensity profiles of neither well-connected and poorly connected nor iron-rich and nominal-abundance events are appreciably and systematically distinct in their early stages as observed at 1 AU.

(ii) The modelled time scaling of the event, b, displays at least some dependence on β and λ, as well as possibly a faint dependence on ϕ. It typically increases when β and λ increase, pointing to a trend for the event to last longer in relative terms as the magnetic connection between the particle source and the observer becomes weaker. A very similar tendency is apparent when the event rise time τ_{rise} and the delay between the event-related flare onset and modelled event intensity maximum, t_{max}, are considered as functions of β and λ.

(iii) b tends to be larger for nominal-abundance than for iron-rich events, meaning that the former often exhibit a profile that is less impulsive in overall shape, especially with respect to the intensity decay after the maximum is reached. This result independently suggests that, notwithstanding (i), there is a relationship between the Fe/C ratio and the importance of particle acceleration mechanisms: for iron-rich events, a significant proportion of the particle acceleration likely occurs in conjunction with the flare and the initial particle injection as opposed to subsequent stages of the event, whereas for events with a nominal element abundance ratio, the post-flare phase is relatively more pronounced. However, this alone does not mean that protons in iron-rich events are accelerated in flares but that the acceleration is temporally connected to the early phases of the event.

Seeing as the magnetic connection can reasonably be assumed to affect the shape of the event time-intensity profile, (i) is an unanticipated result in that a certain correlation between a and the angles measuring the connectivity is absent. Indeed, to explain satisfactorily the diversity of the shapes of SEP event time-intensity profiles at the Earth, an involved modelling effort that goes well beyond simple observable variables and correlations (such as examining, say, the solar longitude of the event-related flare as a function of a) seems to be necessary. From a practical point of view, such an approach might be beneficial for the field of space weather prediction in particular; the results presented in this work are, as such, of a somewhat more limited applicability than envisaged in that respect.

In contrast to (i), however, (ii) can be regarded as an expected outcome. The effect of the longitudinal distance between the particle source and the observer on the SEP event profile is well known and has been recognized for a long time (see e.g. Cane et al., 1988), and it can be interpreted to reflect the scattering of SEPs and the longitudinal spreading of the event caused by various acceleration and transport mechanisms that affect the particles after their departure from the source site. While these mechanisms may be complicated in themselves and they additionally interact, magnetic connectivity would nevertheless appear to provide a simple and reasonably workable measure for their overall effect on the time scaling of SEP events.

Allowing that the dichotomy of impulsive versus gradual events is best considered a simplification (Cane et al., 2010), there is another long-established observation that substantial heavy ion enhancements (Fe in particular) are typical for impulsive events (Reames, 1988; Reames, 1993, and others). The events of this category characteristically display Fe/C ratios that may exceed those of gradual events by an order of magnitude (Reames, 1995; Raukunen et al., 2016). Short event duration, which can be regarded as an impulsive feature, is therefore expected to be more often associated with iron-rich events than with nominal-abundance events, and (iii) indeed conforms to this expectation. In events such as these, the dominant particle acceleration is currently thought to occur in closed magnetic loops in flares and also at magnetic reconnection sites in solar jets where open field lines are present (Reames, 2021, and references therein).

An interesting and potentially fruitful—as well as fairly straightforward—avenue of further research would be to extend the analysis to higher proton energies, for instance 25—50 MeV. Because protons at these kinetic energies can be presumed to undergo less scattering in interplanetary space, a clearer picture might emerge as to the initial particle injection and acceleration. On the other hand, some of the smallest events included in this work may no

longer be properly analysable at energies much greater than 20 MeV, so there is a possibility that such a follow-up study would have to contend with generally diminished statistics and/or extended event list. It would be desirable, even if probably onerous, additionally to apply some sort of computational modelling to estimate the effects of various SEP transport phenomena on the intensity profile of each individual event. This might allow one to understand better which observed features of the intensity profiles are due to the initial particle acceleration and which features arise later.

Declaration of Competing Interest

The authors declare that they have no known competing financial interests or personal relationships that could have appeared to influence the work reported in this paper.

Acknowledgments

This study has been conducted under the framework of Finnish Centre of Excellence for Research in Sustainable Space (FORESAIL). We acknowledge funding from the European Union's Horizon 2020 research and innovation programme under grant agreement No 101004159 (SERPENTINE) and ESA Contract No. 4000120480/NL/LF/hh "Solar Energetic Particle (SEP) Advanced Warning System (SAWS)".

Appendix A. Description of the analytical function fitting process

The function defined in Eq. 1 was fitted to the natural logarithms of the observed proton intensity data after the data were normalized so that $F(t) = 1$ at the maximum intensity I_{max}. This was defined as the highest measured 5-min intensity during the time range of interest (see below). To perform the fits, we used the Levenberg–Marquardt algorithm implemented for the IDL programming language as the freely distributable software package MPFIT (Markwardt, 2009). In addition to the values of the fit parameters themselves, MPFIT can also calculate and return error estimates for them, and these were applied in our analysis.

Data were included in the fit starting from $t = -5.0$ h and continuing either to event end, start of the next notable and clearly separate intensity rise (indicating another event component or SEP injection), or until a reasonable, visually estimated point in time was reached where the intensity had declined considerably after the maximum. In any case, all data points after $t = 36.0$ h were ignored. The statistical relative error of the measured intensity, which was not available in the data set, was estimated as $\exp(0.20) - 1 \approx 0.22$ for the time interval between 2.0 h before and 4.0 h after the tabulated (nominal) event onset, so as to ensure that the onset and rise phase of the event were emphasized in the function fitting process, and $\exp(0.30) - 1 \approx 0.35$ for the rest of the data selection.

The Levenberg–Marquardt algorithm requires initial guesses for the fit function parameter values. Thus, for every event of interest, a matrix of $9 \times 9 \times 7 \times 12 \times 8$ elements was created to hold the initial guesses for the fit function parameter values ($a, b, t_0, I_0/I_{max}$, and F_{bg}/I_{max}, in this order). Multiple starting guesses are necessary because there is in general no guarantee that a fitting attempt based on a single guess will converge to the global minimum of the χ^2; instead, it may lead to different local minima, depending on the starting point in the phase space.

For a and b, the initial guess values were obtained as follows:

- The data sets for a and b given in Kahler and Ling (2017) were plotted as functions of the solar longitude ϕ of the event-related flare.
- Applying the least squares method, quadratic curves were fitted to these plots, which yielded a coarse estimate for the behaviour of the a and b parameters as functions of solar longitude, $a(\phi)$ and $b(\phi)$.
- The a and b data sets were detrended with $a(\phi)$ and $b(\phi)$, respectively, and the standard deviations for the detrended sets, σ_a and σ_b, were calculated.
- The aforementioned results were used to create two vectors for the initial guesses for a and b, $\{a(\phi) - 1.0\sigma_a, a(\phi) - 0.75\sigma_a, \ldots a(\phi) + 1.0\sigma_a\}$ and $\{b(\phi) - 1.0\sigma_b, b(\phi) - 0.75\sigma_b, \ldots b(\phi) + 1.0\sigma_b\}$.

Fixed values were used for t_0 (namely, $\{-1.99, -1.5, -1.0, 0.0, 3.0, 10.0, 18.0\}$ hours) and I_0/I_{max} ($\{0.8, 0.9, 1.0, 1.1, 1.2, 1.5, 1.8, 2.0, 3.0, 4.0, 6.0, 8.0\}$). For F_{bg}/I_{max}, the arithmetic mean of three lowest normalized intensities measured during the pre-event was calculated as F_{low}; this was then used to populate the initial guess vector of $\{0.5F_{low}, 0.7F_{low}, 0.8F_{low}, 0.9F_{low}, 1.0F_{low}, 1.1F_{low}, 1.2F_{low}, 1.5F_{low}\}$.

A function fit to the event data was attempted with every combination of the initial guesses, and the χ^2 statistic divided by the degrees of freedom (DoF) for the resulting fit to the natural logarithms of the normalized intensity measurements (if mathematically successful, in that the algorithm found a converging solution) was recorded for each attempt. The fit with the lowest χ^2/DoF value was selected as best representing the time-intensity profile of the event.

All of the five fit function parameters were constrained a priori in an effort to exclude unphysical or doubtful results. The range of allowed values was $[-7.0, -0.1]$ for a, $(0, 500.0]$ hours for b, $[-2.0, 78.0]$ hours for t_0, $[0.2, 10.0]$ for I_0/I_{max}, and $(0.0, 1.0]$ for F_{bg}/I_{max}. It was considered that any physically meaningful fit would fall well within these limits. In particular, I_0/I_{max} is expected to be close to unity for all successful and meaningful fits, but very large and very small values were notionally allowed to improve the

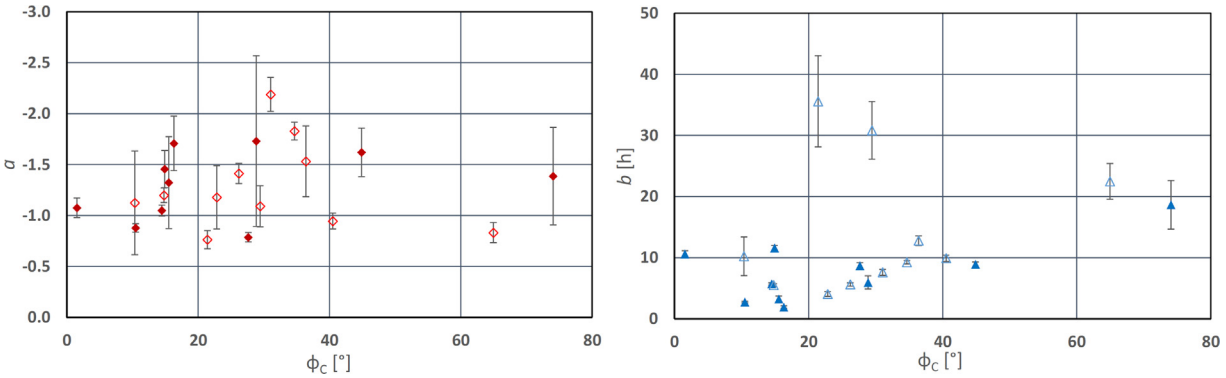

Fig. B.1. Function fit parameters a (left-hand panel) and b (in hours; the right-hand panel) plotted against the connection angle ϕ_C (in degrees) for the studied events. Filled symbols represent events with a high Fe/C ratio ($\geqslant 0.8$), while hollow symbols represent events with nominal Fe/C ratio (< 0.8). The vertical bars denote the statistical 1-σ errors. Events 2, 8, and 12 feature excessive uncertainties with respect to b and are not shown.

chances of the algorithm converging even in cases where the time-intensity profile of the event exhibits momentary high spikes or other such features that complicate modelling.

Appendix B. Connection angles as an alternate measure of magnetic connectivity

In an effort to test and verify our results further and also to compare the relative merits of the PFSS against a somewhat simpler, widely used measure, we carried out a brief supplementary analysis where the PFSS-derived angles α, β, and λ (see Section 2) were replaced with the so-called connection angle, ϕ_C. This angle is the longitudinal distance on the solar surface between the event-related flare and the footpoint of the Parker spiral connecting the observer to the Sun. It can be defined as $\phi_C = \mid \phi - \phi_{foot} \mid$, where ϕ_{foot} is the longitude of the Parker spiral footpoint. In turn, ϕ_{foot} can be calculated as

$$\phi_{foot} = \omega_{\odot} \frac{r_{obs}}{u_{SW}}, \tag{B.1}$$

where $\omega_{\odot}$ is the angular speed of the rotation of the Sun at its equator, r_{obs} is the radial distance between the observer and the Sun, and u_{SW} denotes the solar wind speed. To determine the latter, we used proton data from the Solar Wind Electron, Proton and Alpha Monitor (SWEPAM; McComas et al., 1998) aboard the Advanced Composition Explorer (ACE).[4] We calculated u_{SW} for each event by averaging over the measurements obtained during the six hours preceding and following the tabulated event onset.

Fig. B.1 shows the function fit parameters a (the left-hand panel) and b (in hours; the right-hand panel) plotted as functions of ϕ_C. Considered qualitatively, these results are in good agreement with those obtained using the magnetic angles β and λ in Section 3 but do not reveal any new features: no discernible correlation exists between a and the connection angle, whereas in the case of b, a distribution is seen that suggests a positive correlation. There is again a fair amount of scatter, as well as a number of outlying data points, which also tend to feature the largest statistical uncertainties. While a more in-depth study would be required to find out exhaustively the possible advantages of performing this kind of an analysis with ϕ_C in addition to (or instead of) β and λ, ϕ_C nevertheless appears to offer no immediately obvious benefits over the latter two angles as a measure of magnetic connectivity in this context.

Appendix C. Comparison of event time-intensity profiles based on ERNE and RDS data

As stated in Section 2, an important consideration in choosing the RDS proton intensity data in preference to comparable SOHO/ERNE data as the basis of our work was the absence of gaps in the former. However, SOHO/ERNE data do have certain noteworthy advantages over RDS, most prominently a lower background intensity and better measurement statistics, which should enable smaller SEP events to be detected and analysed. To ascertain that our choice was justified in that the shapes of the time-intensity profiles of the studied events are not strongly dependent on which data set is used, we repeated the function fitting process described in Section 3 and Appendix A for the events listed in Table 1 so that RDS data were replaced with ERNE proton intensity data.

In order to maintain consistency and comparability, statistical weighting was performed identically to the analysis carried out on RDS data. Thus, the intensity measuring error was taken as exp(0.20) − 1 for the initial phase of the event and as exp(0.30) – 1 for the rest (as opposed to an error estimate obtained from particle counts, which are available for ERNE data but not for RDS). Initially included in this comparison were all of the 25 SEP events that yielded an acceptable function fit with RDS. However, in five cases, serious gaps in ERNE data made analysing the event profile impossible, and in two cases, the fit was very poor from a statistical viewpoint; these were omitted from further analysis, leaving 18 successfully fitted profiles.

[4] These data are publicly available at http://www.srl.caltech.edu/ACE/ASC/level2/lvl2DATA_SWEPAM.html.

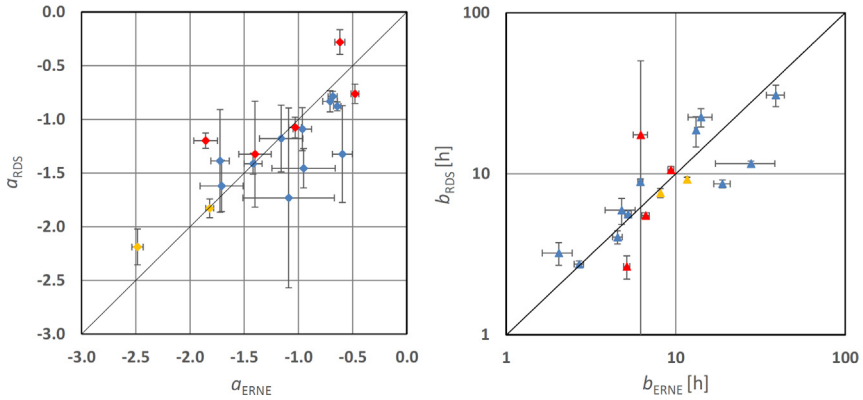

Fig. C.1. Fit parameter a derived from RDS data versus a derived from ERNE data (left-hand panel), and b derived from RDS data versus b derived from ERNE data (right-hand panel). Blue symbols: good fits; yellow symbols: fits with fixed t_0; red symbols: poor fits (see text). The horizontal and vertical bars denote the statistical 1-σ errors. One poor fit, for which $b \approx 160$ h, is not shown in the right-hand panel.

Eleven of the 18 successful cases were considered "good", i.e. they produced a physically meaningful fit with χ^2/DoF less than about unity. Five others where $1.5 \lesssim \chi^2/\mathrm{DoF} \lesssim 3.0$ but where the fit was visually judged to be still acceptable were retained, albeit labelled "poor". Furthermore, the fit routine tended to drive t_0 to its lower limit for events 10 and 16, but these could be fitted satisfactorily when t_0 was fixed at a small value larger than -2.0 h (-1.9 h was used here). Although any event falling into either of the latter two categories would have been rejected in the previous stages of our study, both the "poor" fits and the fits involving a fixed t_0 are included in the following for the sake of completeness.

Fig. C.1 shows the fit parameters a and b as derived from RDS data (a_{RDS} and b_{RDS}, respectively) as functions of these parameters derived from ERNE data (a_{ERNE} and b_{ERNE}). While the statistical limitations should be noted—a considerable amount of scatter is present, several data points feature large statistical errors, and there are rather few data points overall— together with what would seem to be a very faint preference by a_{ERNE} for smaller absolute values than a_{RDS} in well-fitted events, it appears that no large, systematical differences in general exist between the results obtained with RDS and ERNE proton data when these two essential fit parameters are considered. The values of a_{RDS} and a_{ERNE} on one hand and b_{RDS} and b_{ERNE} on the other fall mainly within about two standard deviations of each other, and although some events with larger differences are present, these are for the most part isolated cases. It therefore seems reasonable to assume that the selection of one data set instead of the other is unlikely to affect the results or the final conclusions presented in this work in a substantial manner.

References

Altschuler, M.D., Newkirk, G., 1969. Magnetic fields and the structure of the solar corona. I: methods of calculating coronal fields. Sol. Phys. 9, 131–149.

Barcewicz, S., 2019. Magnetic connectivity in SEP events. Department of Physics and Astronomy, University of Turku, Master's thesis.

van den Berg, J., Strauss, D.T., Effenberger, F., 2020. A primer on focused solar energetic particle transport. Space Sci. Rev. 216, 1–57.

Bieber, J.W., Droege, W., Evenson, P.A., Pyle, R., Ruffolo, D., Pinsook, U., Tooprakai, P., Rujiwarodom, M., Khumlumlert, T., Krucker, S., 2002. Energetic particle observations during the 2000 July 14 solar event. Astrophys. J. 567, 622.

Cane, H.V., Reames, D.V., von Rosenvinge, T.T., 1988. The role of interplanetary shocks in the longitude distribution of solar energetic particles. J. Geophys. Res. 93, 9555–9567.

Cane, H.V., Richardson, I.G., von Rosenvinge, T.T., 2010. A study of solar energetic particle events of 1997–2006: Their composition and associations. J. Geophys. Res. (Space Phys.) 115, A08101.

Crosby, N., Heynderickx, D., Jiggens, P., Aran, A., Sanahuja, B., Truscott, P., Lei, F., Jacobs, C., Poedts, S., Gabriel, S., Sandberg, I., Glover, A., Hilgers, A., 2015. SEPEM: A tool for statistical modeling the solar energetic particle environment. Space Weather 13, 406–426.

Dalla, S., Marsh, M.S., Laitinen, T., 2015. Drift-induced deceleration of solar energetic particles. Astrophys. J. 808, 62.

Desai, M., Giacalone, J., 2016. Large gradual solar energetic particle events. Living Rev. Sol. Phys. 13, 1–132.

Desai, M.I., Mason, G.M., Gold, R.E., Krimigis, S.M., Cohen, C., Mewaldt, R.A., Mazur, J.E., Dwyer, J.R., 2006. Heavy-Ion elemental abundances in large solar energetic particle events and their implications for the seed population. Astrophys. J. 649, 470.

Dröge, W., 2000. Particle Scattering by Magnetic Fields. Cosmic Rays and Earth, pp. 121–151.

Dröge, W., Kartavykh, Y., Klecker, B., Kovaltsov, G., 2010. Anisotropic three-dimensional focused transport of solar energetic particles in the inner heliosphere. Astrophys. J. 709, 912.

Giacalone, J., Jokipii, J.R., 1999. The transport of cosmic rays across a turbulent magnetic field. Astrophys. J. 520, 204–214.

Giacalone, J., Jokipii, J.R., 2012. The longitudinal transport of energetic ions from impulsive solar flares in interplanetary space. Astrophys. J. Lett. 751, L33.

Kahler, S.W., Ling, A.G., 2017. Characterizing solar energetic particle event profiles with two-parameter fits. Sol. Phys. 292, 59.

Kong, X., Guo, F., Chen, Y., Giacalone, J., 2019. The acceleration of energetic particles at coronal shocks and emergence of a double power-law feature in particle energy spectra. Astrophys. J. 883, 49.

Kong, X., Guo, F., Giacalone, J., Li, H., Chen, Y., 2017. The acceleration of high-energy protons at coronal shocks: the effect of large-scale streamer-like magnetic field structures. Astrophys. J. 851, 38.

Kouloumvakos, A., Kwon, R., Rodríguez-García, L., Lario, D., Dresing, N., Kilpua, E., Vainio, R., Török, T., Plotnikov, I., Rouillard, A.,

et al., 2019. The first widespread solar energetic particle event of solar cycle 25 on 2020 November 29-Shock wave properties and the wide distribution of solar energetic particles. Astron. Astrophys. 660, A84.
Kozarev, K., Nedal, M., Miteva, R., Dechev, M., Zucca, P., 2022. A multi-event study of early-stage SEP acceleration by CME-driven shocks—Sun to 1 AU. Front. Astron. Space Sci. 9, 801429.
Kozarev, K.A., Evans, R.M., Schwadron, N.A., Dayeh, M.A., Opher, M., Korreck, K.E., van der Holst, B., 2013. Global numerical modeling of energetic proton acceleration in a coronal mass ejection traveling through the solar corona. Astrophys. J. 778, 43.
Lario, D., Aran, A., Gómez-Herrero, R., Dresing, N., Heber, B., Ho, G. C., Decker, R.B., Roelof, E.C., 2013. Longitudinal and radial dependence of solar energetic particle peak intensities: STEREO, ACE, SOHO, GOES, and MESSENGER observations. Astrophys. J. 767, 41.
Lario, D., Kwon, R.-Y., Vourlidas, A., Raouafi, N., Haggerty, D., Ho, G., Anderson, B., Papaioannou, A., Gómez-Herrero, R., Dresing, N., et al., 2016. Longitudinal properties of a widespread solar energetic particle event on 2014 February 25: evolution of the associated CME sshock. Astrophys. J. 819, 72.
Lario, D., Raouafi, N., Kwon, R.-Y., Zhang, J., Gómez-Herrero, R., Dresing, N., Riley, P., 2014. The solar energetic particle event on 2013 April 11: an investigation of its solar origin and longitudinal spread. Astrophys. J. 797, 8.
Laurenza, M., Consolini, G., Storini, M., Damiani, A., 2015. The Weibull functional form for SEP event spectra. J. Phys: Conf. Ser. 632, 012066.
Markwardt, C.B., 2009. Non-linear Least-squares Fitting in IDL with MPFIT. In: Bohlender, D.A., Durand, D., Dowler, P. (Eds.), Astronomical Data Analysis Software and Systems XVIII ASP Conference Series, Vol. 411, proceedings of the conference held 2–5 November 2008 at Hotel Loews Le Concorde, Québec City, QC, Canada. Edited by David A. Bohlender, Daniel Durand, and Patrick Dowler. San Francisco: Astronomical Society of the Pacific, 2009, p. 251. volume 411 of Astronomical Society of the Pacific Conference Series.
McComas, D.J., Bame, S.J., Barker, P., Feldman, W.C., Phillips, J.L., Riley, P., Griffee, J.W., 1998. Solar wind electron proton alpha monitor (SWEPAM) for the advanced composition explorer. Space Sci. Rev. 86, 563–612.
Mishev, A.L., 2014. Computation of radiation environment during ground level enhancements 65, 69 and 70 at equatorial region and flight altitudes. Adv. Space Res. 54, 528–535.
Paassilta, M., Papaioannou, A., Dresing, N., Vainio, R., Valtonen, E., Heber, B., 2018. Catalogue of > 55 MeV Wide-longitude Solar Proton Events Observed by SOHO, ACE, and the STEREOs at ≈1 AU During 2009–2016. Sol. Phys. 293, 70.
Papaioannou, A., Sandberg, I., Anastasiadis, A., Kouloumvakos, A., Georgoulis, M.K., Tziotziou, K., Tsiropoula, G., Jiggens, P., Hilgers, A., 2016. Solar flares, coronal mass ejections and solar energetic particle event characteristics. J. Space Weather Space Climate 6, A42.
Pomoell, J., Aran, A., Jacobs, C., Rodríguez-Gasén, R., Poedts, S., Sanahuja, B., 2015. Modelling large solar proton events with the shock-and-particle model. Extraction of the characteristics of the MHD shock front at the cobpoint. J. Space Weather Space Climate 5, A12.
Raukunen, O., Valtonen, E., Vainio, R., 2016. Iron-rich solar particle events measured by SOHO/ERNE during two solar cycles. Astron. Astrophys. 589, A138.
Reames, D.V., 1988. Bimodal abundances in the energetic particles of solar and interplanetary origin. Astrophys. J. 330, L71.
Reames, D.V., 1993. Non-thermal particles in the interplanetary medium. Adv. Space Res. 13, 331–339.
Reames, D.V., 1995. Coronal abundances determined from energetic particles. Adv. Space Res. 15, 41–51.
Reames, D.V., 2013. The two sources of solar energetic particles. Space Sci. Rev. 175, 53–92.
Reames, D.V., 2019. Element Abundances of solar energetic particles and the photosphere, the corona, and the solar wind. Atoms 7, 104.
Reames, D.V., 2021. Sixty years of element abundance measurements in solar energetic particles. Space Sci. Rev. 217, 72.
Rouillard, A.P., Odstrčil, D., Sheeley, N.R., Tylka, A., Vourlidas, A., Mason, G., Wu, C.C., Savani, N.P., Wood, B.E., Ng, C.K., Stenborg, G., Szabo, A., St. Cyr, O.C., 2011. Interpreting the properties of solar energetic particle events by using combined imaging and modeling of interplanetary shocks. Astrophys. J. 735, 7.
Sandberg, I., Jiggens, P., Heynderickx, D., Daglis, I.A., 2014. Cross calibration of NOAA GOES solar proton detectors using corrected NASA IMP-8/GME data. Geophys. Res. Lett. 41, 4435–4441.
Schrijver, C.J., De Rosa, M.L., 2003. Photospheric and heliospheric magnetic fields. Sol. Phys. 212, 165–200.
Torsti, J., Valtonen, E., Lumme, M., Peltonen, P., Eronen, T., Louhola, M., Riihonen, E., Schultz, G., Teittinen, M., Ahola, K., Holmlund, C., Kelhä, V., Leppälä, K., Ruuska, P., Strömmer, E., 1995. Energetic particle experiment ERNE. Sol. Phys. 162, 505–531.
Tylka, A., Cohen, C., Dietrich, W., Lee, M., Maclennan, C., Mewaldt, R., Ng, C., Reames, D., 2005. Shock geometry, seed populations, and the origin of variable elemental composition at high energies in large gradual solar particle events. Astrophys. J. 625, 474.
Vainio, R., Desorgher, L., Heynderickx, D., Storini, M., Flückiger, E., Horne, R.B., Kovaltsov, G.A., Kudela, K., Laurenza, M., McKenna-Lawlor, S., Rothkaehl, H., Usoskin, I.G., 2009. Dynamics of the Earth's particle radiation environment. Space Sci. Rev. 147, 187–231.
Wijsen, N., Aran, A., Pomoell, J., Poedts, S., 2019. Modelling three-dimensional transport of solar energetic protons in a corotating interaction region generated with EUHFORIA. Astron. Astrophys. 622, A28.